

Defect-Defect Interactions in the Buckling of Imperfect Spherical Shells

Fani Derveni, Arefeh Abbasi, and Pedro M. Reis*
Ecole Polytechnique Fédérale de Lausanne (EPFL)
Flexible Structures Laboratory
CH-1015 Lausanne, Switzerland

We perform finite element simulations to study the impact of defect-defect interactions on the pressure-induced buckling of thin, elastic, spherical shells containing two dimpled imperfections. Throughout, we quantify the critical buckling pressure of these shells using their knockdown factor. We examine cases featuring either identical or different geometric defects and systematically explore the parameter space, including the angular separation between the defects, their widths and amplitudes, and the radius-to-thickness ratio of the shell. As the angular separation between the defects is increased, the buckling strength initially decreases, then increases before reaching a plateau. Our primary finding is that the onset of defect-defect interactions, as quantified by a characteristic length scale associated with the onset of the plateau, is set by the critical buckling wavelength reported in the classic shell-buckling literature. Beyond this threshold, within the plateau regime, the buckling behavior of the shell is dictated by the largest defect.

Dedication: We dedicate this manuscript to Prof. Kyung-Suk Kim, a truly inspiring scholar in our Mechanics community and a beacon of inspiration, rigor, creativity, and intellectual generosity. Prof. Kim’s mastery of opening new research directions and revisiting classic problems, always with fresh eyes, have been a constant source of inspiration for us. The corresponding author is especially grateful to Prof. Kim for the exceptional support, guidance, and mentoring he received over the years.

I. INTRODUCTION

The buckling of elastic shell structures is highly sensitive to imperfections [1–3]; a problem that is relevant across length scales, from viruses [4] and colloidal capsules [5] to large storage tanks [6]. Even if this is a long-standing classic subject [7–18], the past decade has seen a revival in the study of the buckling of shells and their imperfection sensitivity [19]. For a historical perspective and a more thorough contextualization of the modern account of single-defect shell buckling, we direct the reader to Refs. [19–33].

The canonical question, which remains challenging despite decades of research, is: *What are the critical conditions for the buckling of an imperfect shell?* Recently, in an effort to address this question, an experimental technique has been developed for fabricating spherical shells containing a single dimpled imperfection, which can be engineered precisely [34]. Subsequent buckling studies utilizing this model system demonstrated that if the geometry of the imperfection is characterized in detail, the critical pressure can be predicted accurately, either using the Finite Element Method (FEM) or via numerical solutions of the shell-theory equations [35]. The knockdown

factor, defined as the ratio between the critical buckling pressure of the imperfect shell and that of the equivalent perfect one [7], is the commonly used metric in these studies. For realistic shells, predicting the knockdown factor, which is always less than unity, is notoriously challenging.

Beyond the model system of a single-defect shell, we have recently investigated the more realistic case of a large number of geometric imperfections distributed randomly over the surface of a spherical shell [36]. Importantly, we evidenced that given an input log-normal distribution for the amplitude of defects, the resulting knockdown factor is described by a 3-parameter Weibull distribution, a finding that places shell buckling in the broader class of extreme-value statistics phenomena [37–42]. In that study, we also found that interactions between two adjacent defects, depending on the defect-to-defect separation, can potentially strengthen or weaken the shell in comparison to the single-defect case. There is a similar problem for cylindrical shells, both with a single defect [23, 25, 29, 43–45] or distribution of defects [46–49]. Even though there have been some studies on the buckling of cylindrical shells containing two defects [50, 51], to the best of our knowledge, a systematic exploration of defect-defect interactions in the buckling of *spherical* shells has not been tackled to date.

Here, we study the buckling of imperfect hemispherical shells containing two dimpled defects. The geometric properties of these two imperfections can be either identical or different. Methodologically, we conduct FEM simulations, which have been previously validated thoroughly against experiments [36]. First, we focus on how the angular separation between the two defects affects the knockdown factor, characterizing how the interaction regime is impacted by the width and amplitude of the imperfections. Then, we compare the threshold of the defect-defect separation for the onset of interactions to the theoretical prediction of the full wavelength of the classic critical buckling wavelength for a spherical shell [52]. Our main finding is that the arc length associated with the defect-defect interaction threshold depends

* pedro.reis@epfl.ch

directly on the radius-to-thickness ratio of the shell, scaling linearly with this critical buckling wavelength.

Our paper is organized as follows. First, in Sec. II, we define the problem at hand and outline the research questions. Next, in Sec. III, we describe the FEM simulations employed in our study. In Sec. IV, we present a first set of results on the influence of the radius-to-thickness ratio on the buckling behavior of shells containing two defects. More detailed results for shells with identical defects are provided in Sec. V and with different defects in Sec. VI. Finally, in Sec. VII, we summarize the conclusions of our study and offer suggestions for future research directions.

II. PROBLEM DEFINITION

We consider a thin, elastic, and hemispherical shell of radius, R , and thickness, t , as illustrated in Fig. 1(a,b). The shell is clamped at the equator and contains *two* geometric imperfections. In their undeformed configuration, each defect is shaped as a Gaussian dimple, with the following radial deviation from the perfect spherical geometry:

$$\hat{w}_i(\alpha) = -\delta_i e^{-(\alpha/\alpha_i)^2}, \quad (1)$$

where the indices $i = \{1, 2\}$ represent each of the two defects, α is the local angular distance corresponding to each defect (measured from their centers), α_i is the half-angular width of the i th defect, and δ_i is its amplitude (maximum radial deviation of the mid-surface of the shell). The global angular (zenith) coordinate, β , is defined from the pole ($\beta = 0$), where the first defect ($i = 1$) is always located. The other defect is at β_2 . Following conventional practice in shell-buckling studies [10, 53], the defect amplitude of each defect is normalized as $\bar{\delta}_i = \delta_i/t$, while the width is normalized as $\lambda_i = [12(1 - \nu^2)]^{1/4} (R/t)^{1/2} \alpha_i$. Here, ν is the Poisson's ratio of the material. The shell thickness, t , is kept constant throughout so that we focus only on geometric imperfections, unlike previous work on through-thickness defects [28] or elasto-plastic dents [54].

First, we will analyze shells containing two identical defects: $\lambda = \lambda_1 = \lambda_2$ and $\bar{\delta} = \bar{\delta}_1 = \bar{\delta}_2$. Subsequently, we will consider the scenario of two different defects; $\lambda_1 \neq \lambda_2$ and/or $\bar{\delta}_1 \neq \bar{\delta}_2$. Since the $i = 1$ defect is always positioned at the shell pole ($\beta = 0$) and the $i = 2$ defect is at β_2 , the angular separation (center-to-center) between the two defects is $\varphi_{(1,2)} = \beta_2$. To facilitate the discussion on defect-defect interactions later in the manuscript, it is important to define an alternative angular separation:

$$\varphi_{(1,2)}^* = \varphi_{(1,2)} - m \frac{\alpha_1 + \alpha_2}{\sqrt{2}}, \quad (2)$$

where $m = \{1, 2, 3\}$ is an integer. The different values of m correspond to successively excluding wider portions from the core of the defects when considering their angular separation. A more comprehensive discussion on

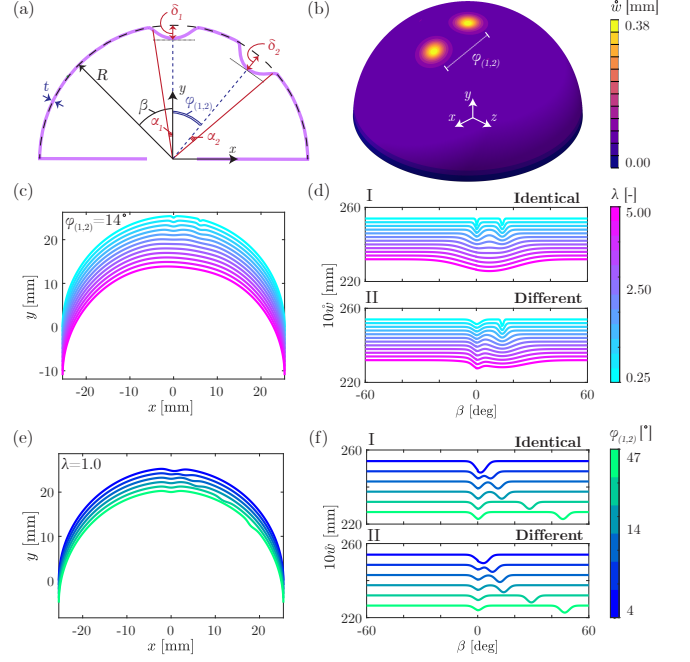


FIG. 1. Reference geometry of the imperfect hemispherical shell with two dimpled defects. (a) 2D schematic, defining all relevant geometric quantities. (b) 3D representation; the shade (see colorbar) represents the radial deviation \hat{w} from a perfect sphere. (c,e) Geometric profiles of identical-defect shells for (c) fixed $\bar{\delta} = 1.5$, $\varphi_{(1,2)} = 14^\circ$ and varying λ_i , and (e) fixed $\bar{\delta} = 1.5$, $\lambda_i = 1.0$ and varying $\varphi_{(1,2)}$. (d,f) Radial deflection, \hat{w} , versus zenith angle, β , for (d) constant $\varphi_{(1,2)} = 14^\circ$ between (dI) identical defects with various λ_i or (dII) different defects with various λ_2 . (f) Similar data, with constant $\lambda_i = 1$, for (fI) identical defects with various $\varphi_{(1,2)}$ or (fII) different defects with various $\varphi_{(1,2)}$. The representative cases for identical defects (dI, fI) have $\bar{\delta}_i = 1.5$, and the different-defects cases (dII, fII) have $\bar{\delta}_1 = 1$, $\bar{\delta}_2 = 1.5$ and $\lambda_1 = 1$. For clarity, all profiles are offset in panels (c,d) by 1 mm, in (e) by 2 mm, and in (f) by 5.5 mm downwards. Also, the \hat{w} profiles in panels (d) are shown with an amplification factor of 10.

this point will be provided in Sec. V. Finally, recalling Eq. (1), the combined profile of a shell with two dimples is

$$\hat{w}(\beta, \theta) = \hat{w}_1(0, 0) + \hat{w}_2(\varphi_{(1,2)}, \theta_2), \quad (3)$$

where β and θ are the *global* zenith and azimuthal spherical (polar) coordinates, respectively.

Figs. 1(c-f) depict representative examples of the mid-surface profile of a shell with $R/t = 100$. These profiles are visualized within the great plane that intersects the shell and passes through the centers of the two imperfections. Note that, given the localized (dimpled) profile in Eq. (3), the shells are *not* axisymmetric, and the profiles shown in Fig. 1 are solely for illustration purposes. Figs. 1(c,e) show the Cartesian profiles in the y - x great plane; for clarity, all profiles are offset vertically (see caption for details). As an alternative representation, the

$\dot{w}(\beta)$ curves in Figs. 1(d,f) correspond to the radial deviation from a perfect hemisphere as a function of the global zenith angle, $\beta \in [-60, 60]^\circ$. These limiting angles are chosen as the maximum location of the defects to avoid interactions with the equator boundary [36]. When their widths, λ_i , are too large (Figs. 1c,d) or when their angular separation, $\varphi_{(1,2)}$, is too small (Figs. 1e,f), the two defects can merge to form a single defect.

Following a similar approach as in previous studies [26, 28, 30, 35, 36], we depressurize the clamped hemispherical shell until buckling occurs. Given the actual critical buckling pressure of the imperfect shell, p_{\max} , the knockdown factor is defined as $\kappa = p_{\max}/p_c$, where p_c is the classic prediction for the respective perfect shell geometry [7, 35]. Our goal is to characterize how κ for a shell with the two-defect geometry specified above depends on the following geometric parameters: $\bar{\delta}_i$, λ_i , $\varphi_{(1,2)}$, and R/t . We will give particular attention to identifying the regimes where the interactions between the two defects induce non-trivial changes in κ .

Our main contribution will be the definition of a threshold arc length for the separation between the two defects, beyond which their interactions become negligible. We will consider two versions of this separation-arc-length threshold: $l_p = R\varphi_{p(1,2)}$, defined from center-to-center of the defect, and $l_p^* = R\varphi_{p(1,2)}^*$, adjusted to account for edge effects of the defects using $\varphi_{(1,2)}^*$ introduced in Eq. (2). We provide evidence that this latter arc-length, with $m = 1$, is set by

$$l_p^* \approx l_c = 2\pi[12(1 - \nu^2)]^{-1/4}\sqrt{Rt}, \quad (4)$$

where l_c , computed in the seminal work by Hutchinson [52], is the theoretical critical buckling wavelength for a spherical shell. More technically, l_c is the full wavelength of the axisymmetric bifurcation mode at the equator of the shell.

In our previous work [36], we presented preliminary evidence for the result in Eq. (4), but only with a single value of $R/t = 110$. Hence, we were unable to fully test Eq. (4). In the present study, we will change this radius-to-thickness ratio within the range $R/t \in [100, 500]$ to examine how l_p^* relates to l_c . Furthermore, in Ref. [36], we reported evidence for the potential interactions between nearby defects and how they can lead to stronger or weaker shells in comparison to single-defect shells. However, the data in that study was limited to a few specific cases. In the present work, we will explore the various geometric parameters of the system systematically and seek to characterize how defect-defect interactions impact κ for spherical shells containing two imperfections.

III. METHODOLOGY: FEM SIMULATIONS

We performed full 3D simulations using the Finite Element Method (FEM) with the commercial software ABAQUS/Standard [55]. In our prior work [33, 36],

we validated this approach against precision experiments similar to the multi-defects geometry considered here. Each quarter of the hemispherical shell is discretized in the meridional and azimuthal using four-noded S4R shell elements: a total of 67500 elements for shells with $R/t \leq 300$ and 187500 elements for shells with $R/t \geq 400$. This level of discretization was deemed suitable after conducting a thorough mesh-convergence analysis. To set the initial geometry of the imperfect shell, we initiated with a perfect hemispherical mesh. Subsequently, we introduced nodal displacements according to the desired profiles of the two imperfections, following Eq. (3), with varying values for the geometric parameters ($\bar{\delta}_i$, λ_i , $\varphi_{(1,2)}$). The shell thickness remained constant throughout the simulations.

The shells were subject to uniform live pressure on their outer surface, while their equator was set as a clamped boundary. We employed a Riks (static) solver with the following parameters for the shells with $R/t \leq 300$: an initial arc length increment of 0.1, a minimum increment of 10^{-5} , and a maximum increment of 0.5. For the thinnest shells with $R/t \geq 400$, the corresponding parameters of the Riks solver were 0.002, 10^{-10} , and 0.2, respectively. Geometric nonlinearities were considered throughout the analysis.

The hemispherical shells were modeled using the material properties of vinylpolysiloxane (VPS-32, Elite Double 32, Zhermack) as a neo-Hookean and incompressible solid; the material had a Poisson's ratio of $\nu \approx 0.5$ and Young's modulus of $E = 1.26$ MPa. These material properties were chosen to match those of previous shell-buckling experiments [26, 28, 30, 35, 36] used to validate our FEM-simulation approach. The geometric parameters of the two-defect imperfect shells were varied in the following ranges: $\bar{\delta}_i \in [0.5, 3]$, $\lambda_i \in [0.25, 5]$, $R/t \in [100, 500]$ (constant $R = 25.4$ mm, varying t) and $\varphi_{(1,2)} \in [1, 60]^\circ$.

IV. HYPOTHESIS FOR THE DEFECT-DEFECT INTERACTION REGIME

We start our investigation by quantifying how the knockdown factor, κ , of the two-defects shells depends on the radius-to-thickness ratio, R/t . Throughout, we will focus on numerical experiments conducted using the FEM simulation approach described in the preceding section.

In Fig. 2, we plot κ versus the defect-defect angular separation, $\varphi_{(1,2)}$, for shells comprising either (a) two identical or (b) two different defects, at several values of R/t . For now, we set the amplitudes and widths of the defects as follows. For the case of identical defects (Fig. 2a), we fixed $\bar{\delta} = 1.5$ and $\lambda = 1$. For the case of different defects (Fig. 2b), we fixed $\bar{\delta}_1 = 1$, $\bar{\delta}_2 = 1.5$ and $\lambda_1 = \lambda_2 = 1$. All curves are non-monotonic as a function of $\varphi_{(1,2)}$: κ first decreases, reaching a minimum (κ_{\min}), then increases to a maximum (κ_{\max}), and subsequently

decreases to a constant plateau value (κ_p). As suggested in Ref. [36], this non-monotonic behavior at small values of $\varphi_{(1,2)}$ arises from defect-defect interactions. By contrast, in the plateau region at large values of $\varphi_{(1,2)}$, the largest defect dominates. Note that the horizontal dashed lines in Fig. 2 correspond to κ values for a single-defect shell with $(\bar{\delta}, \lambda) = (1.5, 1)$ and $R/t = 100$, aligning with the plateaus of all the two-defects curves. The identical-defects shells (Fig. 2a) exhibit higher values of κ_{\max} than the different-defects shells (Fig. 2b), suggesting that defect-defect interactions are less pronounced in the latter case.

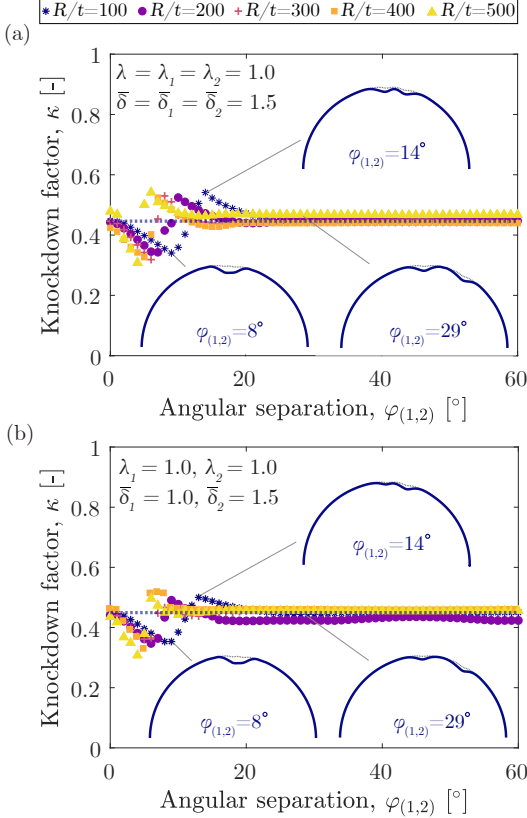


FIG. 2. Knockdown factor, κ , as a function of angular separation, $\varphi_{(1,2)}$, for (a) identical and (b) different defects. The respective values of λ_i and $\bar{\delta}_i$ are provided in the legend of each plot. Shells with varying radius-to-thickness ratio, R/t , are considered, as indicated in the top legend (common to both panels). Insets: Greater-plane profiles of imperfect shells with $R/t = 100$ and different values of $\varphi_{(1,2)}$ in their original configurations (dotted lines) and at the onset of buckling (solid lines). The radial deviation of the latter is amplified by a factor of 3 for visualization purposes. The horizontal dashed lines correspond to the κ values of a single-defect shell with $R/t = 100$ and $(\bar{\delta}, \lambda) = (1.5, 1)$.

To help visualize the buckling process, the insets of Fig. 2 offer representative snapshots of the greater-plane (2D) profiles obtained from the FEM simulations for shells with $R/t = 100$ and various defect-defect angular separations. Near κ_{\min} (e.g., $\varphi_{(1,2)} = 8^\circ$), the two defects

are almost superimposed, resulting in a reduced knock-down factor (cf. Eq. 3). For intermediate separations (e.g., $\varphi_{(1,2)} = 14^\circ$), near κ_{\max} , the region between the two defects acts as a constraint for buckling, leading to higher values of κ . When the two defects are sufficiently far apart (e.g., $\varphi_{(1,2)} = 29^\circ$), in the plateau region, the largest defect dominates the buckling.

All the plotted data sets in Fig. 2, with varying R/t values, exhibit the aforementioned non-monotonic behavior of $\kappa(\varphi_{(1,2)})$. However, as R/t increases, the interaction regions (before the plateau is reached) progressively shift to lower values of $\varphi_{(1,2)}$. This observation highlights the influence of the radius and thickness of the shell on the defect-defect interactions. We hypothesize that the threshold angular separation, below which defects interact and above which the plateau begins, is directly related to \sqrt{Rt} ; the characteristic length scale associated with the balance between bending and stretching effects [30]. Consequently, we anticipate that the onset of the plateau in the $\kappa(\varphi_{(1,2)})$ curves is directly related to the critical buckling wavelength, $l_c \sim \sqrt{Rt}$, as expressed in Eq. (4). Without wanting to spoil a surprise, the results in the next section will confirm this hypothesis.

V. INTERACTIONS BETWEEN TWO IDENTICAL DEFECTS

In this section, we focus solely on imperfect shells with two *identical* defects. The angular separation between their centers, $\varphi_{(1,2)}$, can be recast as the defect-defect separation *arc length*, $l = R\varphi_{(1,2)}$. Our objective is to quantify the dependence of the FEM-computed knock-down factor, κ , for these shells on l , R/t , $\bar{\delta}$, and λ .

In Fig. 3, we present $\kappa(l)$ curves for a shell with $R/t = 100$: in panel (a) for fixed widths ($\lambda = 1$) while varying their amplitudes ($\bar{\delta} \in [0.5, 3]$), and, in (b), for fixed defect amplitudes ($\bar{\delta} = 1.5$) while varying their widths ($\lambda \in [0.25, 5]$). In both plots, the vertical lines represent the critical buckling wavelength for a spherical shell, l_c , provided in Eq. (4) [52], for this shell with $R/t = 100$. Note that l_c does not depend on any of the defect parameters. Fig. 3(a) and Fig. 3(b) both exhibit non-monotonic $\kappa(l)$, indicative of defect-defect interactions, which consistently occur for $l \lesssim l_c$ (shaded region). For $l \gtrsim l_c$, all curves reach a plateau. Naturally, the specific values of κ_{\min} , κ_{\max} , and κ_p depend on the actual defect geometry, as extensively investigated in previous studies for single-defect [24, 33, 35] and many-defects[36] scenarios.

We now select some data from Fig. 3(a), for $\lambda = 1$ and $\bar{\delta} = \{0.5, 1.0, 1.5\}$, and from Fig. 3(b), for $\bar{\delta} = 1.5$ and $\lambda = \{0.5, 1.0, 3.0\}$, and present them in Fig. 4(a) and (b) as a function of the normalized arc length l/l_c . Additional simulation data for $R/t = 200$ and 500 are included. The shaded regions indicate small angular separations where the two defects overlap (cf. the corresponding 2D profiles in Fig. 1). It is remarkable that

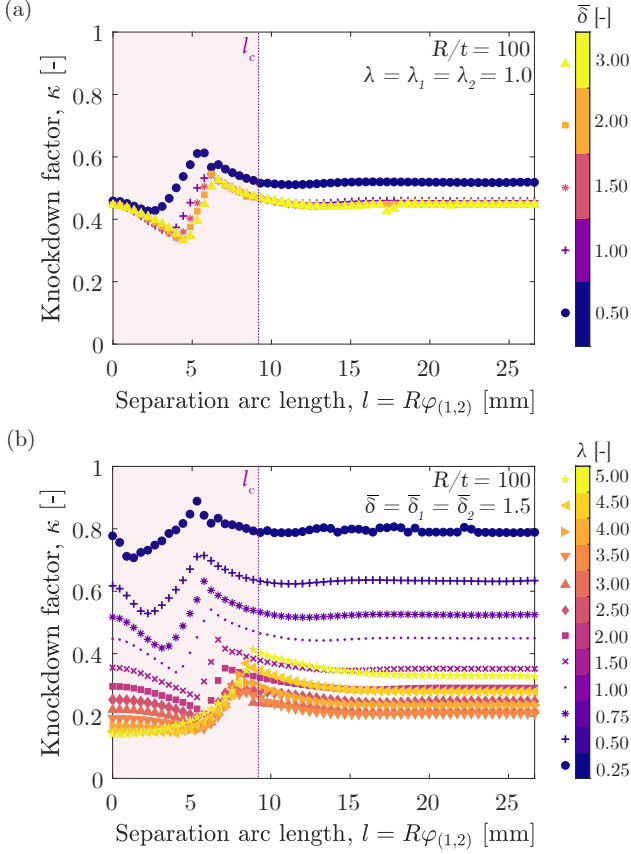


FIG. 3. Knockdown factor, κ , for a shell with $R/t = 100$ as a function of the defect-defect arclength, l , for identical defects. Panel (a): fixed $\lambda = 1$, varying $\bar{\delta} \in [0.5, 3]$. Panel (b): fixed $\bar{\delta} = 1.5$, varying $\lambda \in [0.25, 5]$. Different markers and a color bar distinguish the various parameter values. The vertical dotted line presents the theoretical, critical buckling wavelength, l_c (cf. Eq. 4), for $R/t = 100$.

all the $\kappa(l/l_c)$ data collapse, with the emergence of their plateaus past $l/l_c \gtrsim 1$.

The aforementioned observation regarding the onset of the plateau underscores the importance of the critical buckling wavelength, l_c , in setting the threshold arc length separation for the defect-defect interaction regime. This finding represents an important step in confirming the hypothesis laid out in Sec. IV. To quantify this threshold, we consider the maximum (κ_{\max}) and plateau (κ_p) values of the $\kappa(l)$ curves in Figs. 3 and 4. The threshold separation is defined as the arc length corresponding to the 10% cut-off: $0.1(\kappa_{\max} - \kappa_p)$. An uncertainty of $\pm 0.05(\kappa_{\max} - \kappa_p)$ is assigned to each threshold value to account for the non-sharp onset of the plateau, consistently with the percentual definitions used in previous work [24]. As mentioned in Sec. II, there are two possible definitions for the defects separation arc length, l_p or l_p^* , depending on whether we consider the center-to-center ($\phi_{(1,2)}$) or the adjusted ($\phi_{(1,2)}^*$) angular separations, respectively. The latter excludes a portion from the core

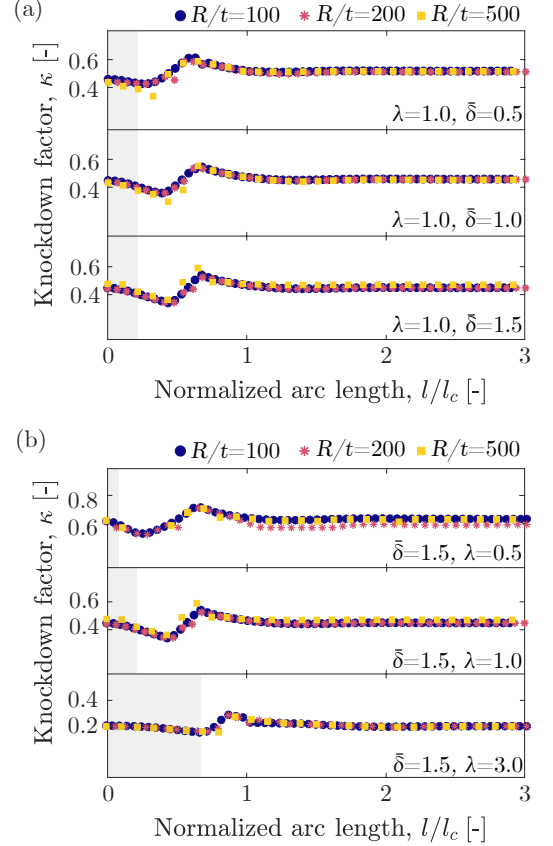


FIG. 4. Knockdown factor, κ , as a function of l/l_c , the defect-defect arc length normalized by the critical buckling wavelength defined in Eq. (4). (a) Constant $\lambda = 1$, varying $\bar{\delta}$. (b) Constant $\bar{\delta} = 1.5$, varying λ . The different markers refer to various radius-to-thickness ratios, R/t . The shaded areas indicate the regions where the defects overlap, resulting in a single larger defect.

of the defects and was defined in Eq. (2). Schematics illustrating these two definitions are provided in Fig. 5 (top).

At this point, it is important to revisit the Gaussian shape (cf. Eq. 1) of the dimpled imperfections we are considering. Note that, at the local angular coordinate of each defect $\alpha = m\alpha_i$, its deviation from the perfect sphere is $\hat{w}_i = -\delta_i e^{-m}$. Also, $\alpha_i/\sqrt{2}$ can be interpreted as the standard deviation of this Gaussian shape, $\hat{w}_i(\alpha)$. Therefore, l_p^* can be seen as excluding some portion of the core of each defect. Taking the values $m = 1, 2$, or 3 corresponds to excluding 68.3%, 95.6%, and 99.7% of the defect, respectively [56]. The choice of m determines the extent to which the core of the defect is excluded, with $m = 3$ effectively considering the edge-to-edge separation between defects. It is important to note that at $\alpha = \alpha_i/\sqrt{2}$, there is an inflection point in Eq. (2) and $\hat{w}_i''(\alpha_i/\sqrt{2}) = 0$.

We have measured l_p or l_p^* as functions of l_c , for shells with $R/t \in [100, 500]$ and two identical defects with

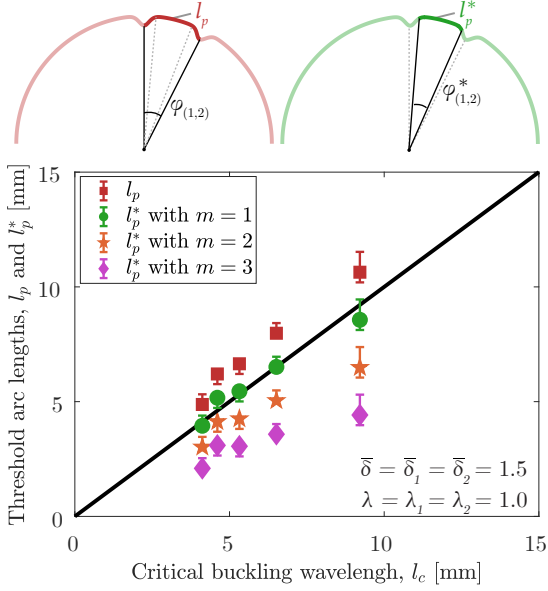


FIG. 5. Threshold arc length separations for the interaction regime, l_p and l_p^* , versus the critical buckling wavelength, l_c , for identical defects with $\bar{\delta} = 1.5$ and $\lambda = 1$. Both $l_p = R\varphi_{(1,2)}$ (squares) and $l_p^* = R\varphi_{(1,2)}^*$ (circles for $m = 1$, pentagons for $m = 2$, and diamonds for $m = 3$) threshold definitions are examined, as illustrated in the 2D schematics (top). The threshold values, l_p and l_p^* are computed as described in the text. The error bars represent $\pm 0.05|\kappa_{\max} - \kappa_p|$. The solid line represents $l_p = l_p^* = l_c$.

$(\bar{\delta}, \lambda) = (1.5, 1.0)$. It is worth noting that the different values of R/t yield different values of l_c according to Eq. (4); specifically, l_c increases as R/t decreases. The results shown in Fig. 5 confirm the hypothesis presented in Sec. IV: there is a clear *linear* scaling between l_p or l_p^* with varying m values (cf. Eq. 2) and l_c . What is more, when using the l_p^* definition with $m = 1$, the data lie on the line $l_p^* = l_c$. This remarkable result demonstrates that the threshold separation for defect-defect interactions is set by the critical buckling wavelength of the shell at the inflection point in the Gaussian profile, $\hat{w}(\alpha_i)$. Hence, for the remainder of our study, we will adopt the definition of l_p^* with $m = 1$.

Having examined the specific geometry for an imperfect shell with $(\bar{\delta}, \lambda) = (1.5, 1.0)$ (albeit with different R/t), we now explore the geometric parameter space more systematically. In Fig. 6(a), we plot l_p^*/l_c as a function of $\bar{\delta}$ (with fixed $\lambda = 1.0$), and in Fig. 6(b) λ (with fixed $\bar{\delta} = 1.5$), for different R/t values (see legend). Overall, the data consistently aligns closely with $l_p^*/l_c = 1$ (horizontal dashed line), especially when $\bar{\delta} \geq 1$ (Fig. 6a) and $\lambda \leq 2.5$ (Fig. 6b). In Fig. 6(a), l_p^*/l_c remains approximately constant for all $\bar{\delta} \in [0.5, 3]$ and all $R/t \in [100, 500]$. As also highlighted in Fig. 3(a), the l_p^*/l_c data lie almost on top of the dashed line, deviating by at most 20% within the entire range of $\bar{\delta}$ that we ex-

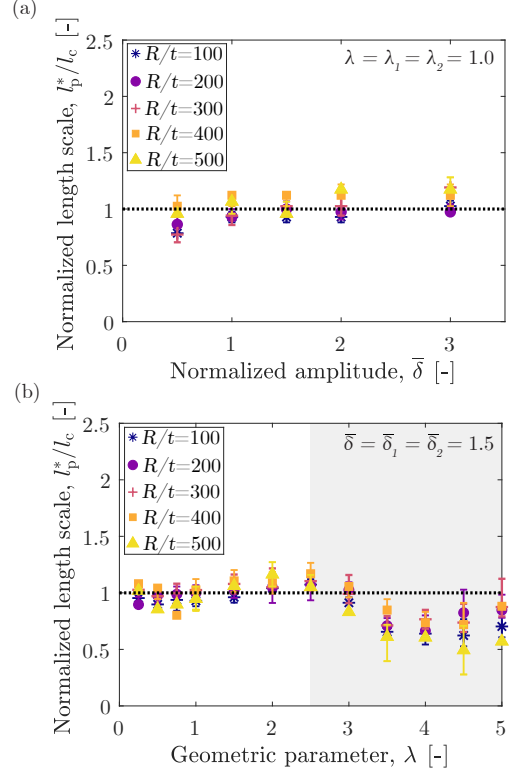


FIG. 6. Normalized threshold defect-defect arclength, l_p^*/l_c , versus (a) normalized amplitude, $\bar{\delta}$, and (b) normalized width, λ , for various values of $R/t \in [100, 500]$. In panel (a), $\lambda = 1$ is kept fixed, and in panel (b), $\bar{\delta} = 1.5$ is fixed. Each marker represents a different value of $R/t \in [100, 500]$, and the horizontal dashed lines correspond to $l_p^* = l_c$. The shaded area in panel (b) highlights the region where defects tend to overlap, forming a single larger defect.

plored. More quantitatively, in Fig. 6(b), for shells with $\lambda \leq 2.5$, the FEM-measured l_p^* is in excellent agreement with the analytical result for l_c , within a 16% difference. For wider defects with $\lambda \geq 2.5$, l_p^* deviates by up to $\approx 50\%$ from l_c . Note that in these shells with wide defects (large λ values), the two defects tend to be nearly juxtaposed, as seen in the profiles in Fig. 1(c) and (d), as well as the shaded region in Fig. 6b (for shells with $R/t = 100$). We attribute the larger deviations of l_p^*/l_c from unity for shells with wide defects to their overlap, which leads to a distorted, imperfect shell geometry.

VI. INTERACTIONS BETWEEN TWO DIFFERENT DEFECTS

In the previous section, we examined shells with two identical defects. Now, we shift our focus to the case of different defects ($\bar{\delta}_1 \neq \bar{\delta}_2$ or $\lambda_1 \neq \lambda_2$). We will fix the geometry of the $i = 1$ defect at the pole with $(\lambda_1, \bar{\delta}_1) = (1.0, 1.0)$, and vary the width (λ_2) and amplitude ($\bar{\delta}_2$) of the second defect.

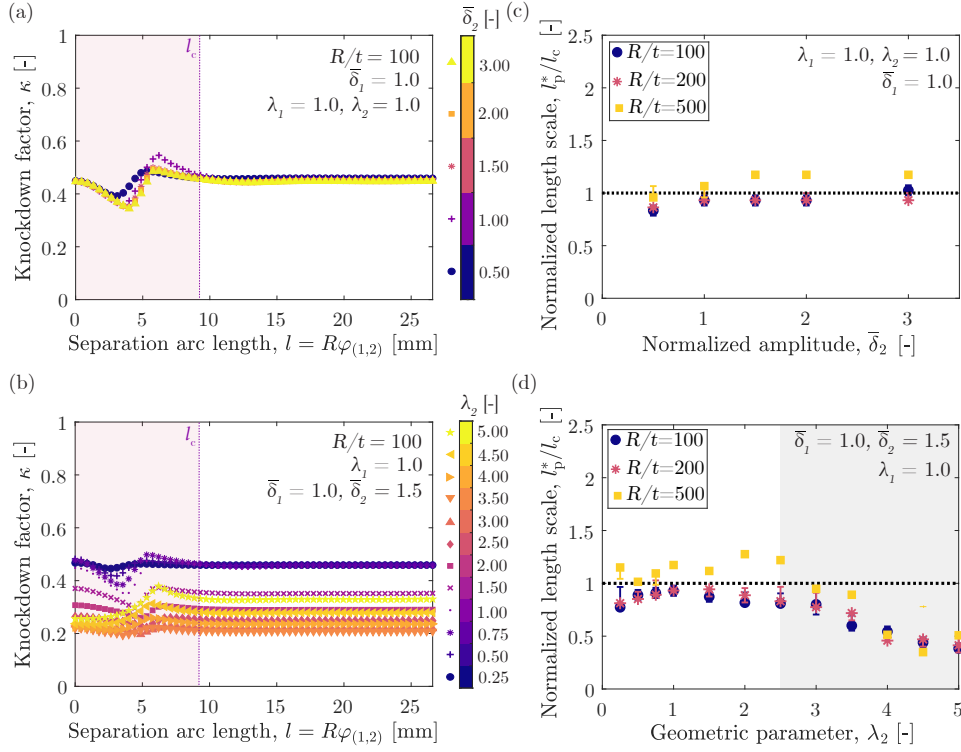


FIG. 7. Knockdown factor, κ , versus arc length, l , for shells with $R/t = 100$. (a) Fixed $\lambda_1 = \lambda_2 = 1$, $\bar{\delta}_1 = 1$ and varying $\bar{\delta}_2 \in [0.5, 3]$. (b) Fixed $\bar{\delta}_1 = 1$, $\bar{\delta}_2 = 1.5$, $\lambda_1 = 1$ and varying $\lambda_2 \in [0.25, 5]$. Normalized arclength, l_p^*/l_c , versus (c) $\bar{\delta}_2$, and (d) λ_2 for $R/t \in [100, 500]$. Different markers and colors are used to represent different (a) $\bar{\delta}_2$, (b) λ_2 , and (c,d) R/t . The vertical dashed lines in panels (a,b) refer to the theoretical prediction of l_c for shells with $R/t = 100$, while the horizontal dashed lines in panels (c,d) represent $l_p^* = l_c$. The shaded region in panel (d) indicates the region where defects overlap, forming a single larger defect (shown for $R/t = 100$, as a representative example).

In Fig. 7(a), we plot the knockdown factor, κ , as a function of defect-defect arc length separation, l , for shells with fixed $R/t = 100$ and $\lambda_2 = 1.0$, while varying $\bar{\delta}_2 \in [0.5, 3]$. These $\kappa(l)$ curves are similar to those for the identical-defects case discussed in Sec. V: κ initially decreases to κ_{\min} , then increases κ_{\max} , before settling to a plateau (κ_p). The exact values of κ_{\min} , κ_{\max} , and κ_p are slightly influenced by the amplitude of the $i = 2$ defect, particularly for $\bar{\delta}_2 = \{0.5, 1.0\}$, but not for $\bar{\delta}_2 > 1.0$, consistent with the known sensitivity of shell buckling to imperfections [35].

In Fig. 7(b), we present $\kappa(l)$ curves for shells with a fixed $R/t = 100$ and $\bar{\delta}_2 = 1.5$, while varying $\lambda_2 \in [0.25, 5]$. The response of these shells is qualitatively different from the behavior described in the previous paragraph, exhibiting three distinct regimes. In the first, when $\lambda_2 \leq 1$, the $\kappa(l)$ curves show the same minimum-maximum-plateau dependence described above and in Sec. V. Since $\lambda_2 > \lambda_1$, the plateau is dictated by the largest ($i = 2$) defect. In the second regime, for $1.5 \leq \lambda_2 \leq 3$, the $\kappa(l)$ curves shift, as a whole, to lower values. While a clear minimum is still observed, the maximum becomes less prominent, tending towards $\kappa_{\max} \rightarrow \kappa_p$. In this regime, the buckling is still dictated by the largest $i = 2$ defect. In the third regime, for $\lambda \geq 3.5$, the $\kappa(l)$

curves shift upwards.

In Fig. 7(a,b), the vertical dotted lines represent the critical buckling wavelength, l_c , defined in Eq. (4), with $R/t = 100$. Similarly to the case of identical defects, we observe that the region (shaded) of interaction for these shells with two different defects lies within $l < l_c$. As in Sec. V, we also compute the normalized threshold for defect-defect interactions (onset of the plateau of the $\kappa(l)$ curves), l_p^*/l_c , for the present case of different defects. These results are presented in Fig. 7(c,d).

In Fig. 7(c), when fixing $\bar{\delta}_1$, λ_1 , and λ_2 , we observe that $l_p^*/l_c \approx 1$ (within 17%) across the whole range of $\bar{\delta}_2$. This finding reinforces that $\bar{\delta}$ is not critical in determining the onset of defect interactions, consistently with the identical-defects case (Fig. 6a). The behavior becomes less straightforward when varying λ_2 while fixing $\bar{\delta}_1$, λ_1 , and $\bar{\delta}_2$, (see Fig. 7d). Here, l_p^*/l_c remains near unity for $\lambda_2 \leq 3$, with a deviation of around 22% for $\lambda_2 \in [0.25, 1]$ and 28% for $\lambda_2 \in [1.5, 3]$. However, when $\lambda_2 \geq 3.5$, l_p^*/l_c progressively drops below unity, reaching approximately 0.4. Recalling the profiles in Fig. 1(d), we note that the edges of the narrow $i = 1$ defect overlap with the wider $i = 2$ defect for larger values of λ_2 . Thus, the shell geometry deviates substantially from a perfect sphere, and the

critical buckling wavelength in Eq. (4) no longer sets the edge of the interaction region. This complex behavior, arising from the increasing overlap of the defects and the nontrivial shell geometries, falls beyond the scope of the present work and warrants further investigation.

Note that, in Fig. 7(c,d), while l_p^*/l_c remains close to unity for intermediate values of λ_2 , the thinnest shells with $R/t = 500$ exhibit notable discrepancies compared to the $R/t = \{100, 200\}$ shells (the results for these two are almost overlapping). We have conducted comprehensive mesh-convergence tests, and it appears that the discrepancies are not due to the discretization. Instead, we attribute these deviations to the higher fluctuations observed in the measured $\kappa(l)$ curves, especially in the plateau region, which in turn affects the measurement of l_p^* using the 10% criterion introduced in Sec. V.

VII. CONCLUSIONS

Using experimentally validated FEM simulations, we investigated the effect of defect-defect interactions on the buckling of pressurized hemispherical shells containing two dimpled imperfections. We examined cases of identical and different defects, varying their geometric parameters (amplitude, δ_i , and width, λ_i) and their relative separation. We measured the knockdown factor (the normalized critical buckling pressure), κ , for these imperfect shells as a function of the angular separation, $\varphi_{(1,2)}$, between their two defects. We then used $\varphi_{(1,2)}$ to define an arc length separation $l = R\varphi_{(1,2)}$. Our findings revealed significant defect-defect interactions when the two defects are in close proximity, leading to non-monotonic behavior in $\kappa(l)$, below a threshold in l . We modified the definition of this interaction threshold, denoted as l_p^* , which corresponds to the inflection point of the Gaussian profile. Beyond l_p^* , the $\kappa(l)$ curves reached a plateau, indicating diminished interactions and the dominance of the largest defect in dictating the knockdown factor.

The main contribution of our study lies in establishing that the onset of defect-defect interactions is determined

by the critical buckling wavelength [52], as $l_p^* \approx l_c$ (cf. Eq. 4). This result is valid for defects with $\lambda_i < 3$, regardless of whether they are identical or different. However, for wider defects, the dimples tend to overlap, and the shell geometry becomes increasingly distorted. The defect amplitude, δ_i , plays a negligible role in setting l_p^* . It is important to note that l_c depends only on the radius, R , and thickness, t , of the shell (other than the Poisson ratio, which was fixed to $\nu = 0.5$ throughout our study).

We hope that our results will stimulate further interest in harnessing defect-defect interactions to enhance the buckling response of spherical shells or inspire the development of novel functional mechanisms derived from these interactions.

ACKNOWLEDGMENTS

We are grateful to John Hutchinson for insightful discussions, which inspired the scope and findings of our study. A comment by him on our previous work [36] was at the source of the hypothesis that l_c dictates the onset of defect-defect interactions. We also thank Michael Gomez for his invaluable feedback on the results presented in this manuscript.

Disclosure on the usage of large language model (LLM)

We used the Large Language Model (LLM) – ChatGPT (GPT-4 architecture, May 12 Version) – in the drafting of this manuscript for grammar and language refinement. We only employed the following two prompts: “fix grammar and typos” and “provide alternative phrasing for.” Nonetheless, all final decisions and content in the manuscript were made and thoroughly reviewed by the authors. As supplementary information, we have included a commented “ \LaTeX diff” version that compares the nearly final draft prior to using ChatGPT with the present final version, noting that the latter also includes several minor edits made by the authors *a posteriori*.

-
- [1] Von Karman, T., and Tsien, H.-S., 1939. “The buckling of spherical shells by external pressure”. *J. Aeronaut. Sci.*, **7**(2), pp. 43–50.
 - [2] Von Karman, T., Dunn, L. G., and Tsien, H.-S., 1940. “The influence of curvature on the buckling characteristics of structures”. *J. Aeronaut. Sci.*, **7**(7), pp. 276–289.
 - [3] Hutchinson, J., Koiter, W., et al., 1970. “Postbuckling theory”. *Appl. Mech. Rev.*, **23**(12), pp. 1353–1366.
 - [4] Lidmar, J., Mirny, L., and Nelson, D. R., 2003. “Virus shapes and buckling transitions in spherical shells”. *Phys. Rev. E*, **68**(5), p. 051910.
 - [5] Datta, S. S., Kim, S.-H., Paulose, J., Abbaspourrad, A., Nelson, D. R., and Weitz, D. A., 2012. “Delayed buckling and guided folding of inhomogeneous capsules”. *Phys. Rev. Lett.*, **109**(13), Sept., p. 134302.
 - [6] Godoy, L. A., 2016. “Buckling of vertical oil storage steel tanks: Review of static buckling studies”. *Thin-Walled Struct.*, **103**, June, pp. 1–21.
 - [7] Zoelly, R., 1915. “Ueber ein knickungsproblem an der kugelschale”. Ph.D. thesis, ETH Zurich, Zurich, Switzerland.
 - [8] Tsien, H.-S., 1942. “A theory for the buckling of thin shells”. *J. Aeronaut. Sci.*, **9**(10), pp. 373–384.
 - [9] Koiter, W. T., 1945. “Over de stabiliteit van het elastisch evenwicht”. Ph.D. thesis, Delft University of Technology, Delft, The Netherlands.
 - [10] Kaplan, A., and Fung, Y. C., 1954. A nonlinear theory of bending and buckling of thin elastic shallow spherical

- shells. Technical Note 3212, National Advisory Committee for Aeronautics, Washington, DC.
- [11] Bijlaard, P., and Gallagher, R., 1960. “Elastic instability of a cylindrical shell under arbitrary circumferential variation of axial stress”. *J. Aerosp. Sci.*, **27**(11), pp. 854–858.
 - [12] Seide, P., Weingarten, V. I., and Morgan, E. J., 1960. The development of design criteria for elastic stability of thin shell structures. Tech. rep., Final Report: STL/TR-60-0000-19425, Space Technology Laboratories, Inc., Los Angeles, CA.
 - [13] Krenzke, M. A., and Kiernan, T. J., 1963. “Elastic stability of near-perfect shallow spherical shells”. *AIAA J.*, **1**(12), pp. 2855–2857.
 - [14] Carlson, R. L., Sendelbeck, R. L., and Hoff, N. J., 1967. “Experimental studies of the buckling of complete spherical shells”. *Exp. Mech.*, **7**(7), Jul, pp. 281–288.
 - [15] Kobayashi, S., 1968. “The influence of the boundary conditions on the buckling load of cylindrical shells under axial compression”. *J. Jpn. Soc. Aeronaut. Eng.*, **16**(170), pp. 74–82.
 - [16] Hutchinson, J. W., Muggeridge, D. B., and Tennyson, R. C., 1971. “Effect of a local axisymmetric imperfection on the buckling behavior of a circular cylindrical shell under axial compression”. *AIAA J.*, **9**(1), pp. 48–52.
 - [17] Budiansky, B., and Hutchinson, J., 1972. “Buckling of circular cylindrical shells under axial compression, in: Contributions to the theory of aircraft structures”. *Delft University Press, Delft, The Netherlands*, pp., pp. 239–259.
 - [18] Babcock, C. D., 1983. “Shell Stability”. *ASME J. Appl. Mech.*, **50**(4b), Dec., pp. 935–940.
 - [19] Gerasimidis, S., Hutchinson, J., Sieber, J., and Thompson, J., 2023. “Foreword to the special issue on new developments in structural stability”. *Philos. Trans. R. Soc. A*, **381**(2244), p. 20220038.
 - [20] Hutchinson, J. W., 2016. “Buckling of spherical shells revisited”. *P. Roy. Soc. A-Math. Phys.*, **472**(2195), p. 20160577.
 - [21] Hutchinson John W., and Thompson J. Michael T., 2017. “Nonlinear buckling behaviour of spherical shells: barriers and symmetry-breaking dimples”. *P. Roy. Soc. A-Math. Phys.*, **375**(2093), May, p. 20160154.
 - [22] Thompson, J. M. T., Hutchinson, J. W., and Sieber, J., 2017. “Probing shells against buckling: a nondestructive technique for laboratory testing”. *Int. J. Bif. Chaos*, **27**(14), p. 1730048.
 - [23] Viot, E., Kreilos, T., Schneider, T. M., and Rubinstein, S. M., 2017. “Stability Landscape of Shell Buckling”. *Phys. Rev. Lett.*, **119**(22), Nov., p. 224101.
 - [24] López Jiménez, F., Marthelot, J., Lee, A., Hutchinson, J. W., and Reis, P. M., 2017. “Technical Brief: Knock-down Factor for the Buckling of Spherical Shells Containing Large-Amplitude Geometric Defects”. *ASME J. Appl. Mech.*, **84**(3), Jan., pp. 034501–034501–4.
 - [25] Gerasimidis, S., Viot, E., Hutchinson, J. W., and Rubinstein, S. M., 2018. “On Establishing Buckling Knock-downs for Imperfection-Sensitive Shell Structures”. *J. Appl. Mech.*, **85**(9), Sept., p. 091010.
 - [26] Marthelot, J., López Jiménez, F., Lee, A., Hutchinson, J. W., and Reis, P. M., 2017. “Buckling of a Pressurized Hemispherical Shell Subjected to a Probing Force”. *ASME J. Appl. Mech.*, **84**(12), Dec., p. 121005.
 - [27] Lee, A., Yan, D., Pezzulla, M., Holmes, D. P., and Reis, P. M., 2019. “Evolution of critical buckling conditions in imperfect bilayer shells through residual swelling”. *Soft Matter*, **15**(30), pp. 6134–6144.
 - [28] Yan, D., Pezzulla, M., and Reis, P. M., 2020. “Buckling of pressurized spherical shells containing a through-thickness defect”. *J. Mech. Phys. Solids*, **138**, p. 103923.
 - [29] Yadav, K. K., Cuccia, N. L., Viot, E., Rubinstein, S. M., and Gerasimidis, S., 2021. “A nondestructive technique for the evaluation of thin cylindrical shells’ axial buckling capacity”. *ASME J. Appl. Mech.*, **88**(5).
 - [30] Abbasi, A., Yan, D., and Reis, P. M., 2021. “Probing the buckling of pressurized spherical shells”. *J. Mech. Phys. Solids*, **155**, p. 104545.
 - [31] Yan, D., Pezzulla, M., Cruveiller, L., Abbasi, A., and Reis, P. M., 2021. “Magneto-active elastic shells with tunable buckling strength”. *Nat. Commun.*, **12**(1), p. 2831.
 - [32] Pezzulla, M., Yan, D., and Reis, P. M., 2022. “A geometrically exact model for thin magneto-elastic shells”. *J. Mech. Phys. Solids*, **166**, p. 104916.
 - [33] Abbasi, A., Derveni, F., and Reis, P., 2023. “Comparing the buckling strength of spherical shells with dimpled versus bumpy defects”. *ASME J. Appl. Mech.*, pp. 1–9.
 - [34] Lee, A., Brun, P.-T., Marthelot, J., Balestra, G., Gallaire, F., and Reis, P., 2016. “Fabrication of slender elastic shells by the coating of curved surfaces”. *Nat. Commun.*, **7**, p. 11155.
 - [35] Lee, A., López Jiménez, F., Marthelot, J., Hutchinson, J. W., and Reis, P. M., 2016. “The geometric role of precisely engineered imperfections on the critical buckling load of spherical elastic shells”. *ASME J. Appl. Mech.*, **83**(11), p. 111005.
 - [36] Derveni, F., Gueissaz, W., Yan, D., and Reis, P. M., 2023. “Probabilistic buckling of imperfect hemispherical shells containing a distribution of defects”. *Philos. Trans. R. Soc. A*, **381**(2244), p. 20220298.
 - [37] Fisher, R. A., and Tippett, L. H. C., 1928. “Limiting forms of the frequency distribution of the largest or smallest member of a sample”. In *Math. Proc. Cambridge Philos. Soc.*, Vol. 24, pp. 180–190.
 - [38] Weibull, W., 1939. “The phenomenon of rupture in solids”. *IVA Handlingar*, **153**.
 - [39] Weibull, W., 1951. “A statistical distribution function of wide applicability”. *J. Appl. Mech.*
 - [40] Jayatilaka, A. D. S., and Trustrum, K., 1977. “Statistical approach to brittle fracture”. *J. Mater. Sci.*, **12**(7), July, pp. 1426–1430.
 - [41] Bažant, Z. P., Le, J.-L., and Bazant, M. Z., 2009. “Scaling of strength and lifetime probability distributions of quasibrittle structures based on atomistic fracture mechanics”. *Proc. Natl. Acad. Sci. U.S.A.*, **106**(28), pp. 11484–11489.
 - [42] Le, J.-L., Ballarín, R., and Zhu, Z., 2015. “Modeling of probabilistic failure of polycrystalline silicon mems structures”. *J. Am. Ceram.*, **98**(6), pp. 1685–1697.
 - [43] Hutchinson, J., 1965. “Buckling of imperfect cylindrical shells under axial compression and external pressure”. *AIAA journal*, **3**(10), pp. 1968–1970.
 - [44] Kyriakides, S., and Ju, G., 1992. “Bifurcation and localization instabilities in cylindrical shells under bending—i. experiments”. *Int. J. Solids Struct.*, **29**(9), pp. 1117–1142.
 - [45] Groh, R., and Pirrera, A., 2023. “Probing the stability landscape of cylindrical shells for buckling knock-

- down factors”. *Philos. Trans. R. Soc. A*, **381**(2244), p. 20220032.
- [46] Amazigo, J. C., 1969. “Buckling under axial compression of long cylindrical shells with random axisymmetric imperfections”. *Q. Appl. Math.*, **26**(4), pp. 537–566.
 - [47] Elishakoff, I., and Arbocz, J., 1982. “Reliability of axially compressed cylindrical shells with random axisymmetric imperfections”. *Int. J. Solids Struct.*, **18**(7), pp. 563–585.
 - [48] Elishakoff, I., and Arbocz, J., 1985. “Reliability of axially compressed cylindrical shells with general nonsymmetric imperfections”. *ASME J. Appl. Mech.*, **52**, pp. 122–8.
 - [49] Elishakoff, I., 2012. “Probabilistic resolution of the twentieth century conundrum in elastic stability”. *Thin-Walled Struct.*, **59**, pp. 35–57.
 - [50] Wullschleger, L., 2006. “Numerical investigation of the buckling behaviour of axially compressed circular cylinders having parametric initial dimple imperfections”. PhD thesis, ETH Zurich.
 - [51] Fan, H., 2019. “Critical buckling load prediction of axially compressed cylindrical shell based on non-destructive probing method”. *Thin-Walled Struct.*, **139**, pp. 91–104.
 - [52] Hutchinson, J. W., 1967. “Imperfection sensitivity of externally pressurized spherical shells”. *ASME J. Appl. Mech.*, **34**, pp. 49–55.
 - [53] Koga, T., and Hoff, N. J., 1969. “The axisymmetric buckling of initially imperfect complete spherical shells”. *Int. J. Solids Struct.*, **5**(7), pp. 679–697.
 - [54] Gerasimidis, S., and Hutchinson, J. W., 2021. “Dent imperfections in shell buckling: The role of geometry, residual stress, and plasticity”. *ASME J. Appl. Mech.*, **88**(3).
 - [55] ABAQUS, 2014. “Abaqus theory guide”. In *Version 6.14*. Dassault Systems Simulia Corp, USA.
 - [56] Feller, W., 1968. *An introduction to probability theory and its applications*, Vol. 81. John Wiley & Sons.